Article

Deciphering the Role of Key Defects in Sb$_2$Se$_3$, a Promising Candidate for Chalcogenide-Based Solar Cells

Adrien Stoliaroff, Alicia Lecomte, Oleg Rubel, Stéphane Jobic, XiangHua Zhang, Camille Latouche,* and Xavier Rocquefelte*
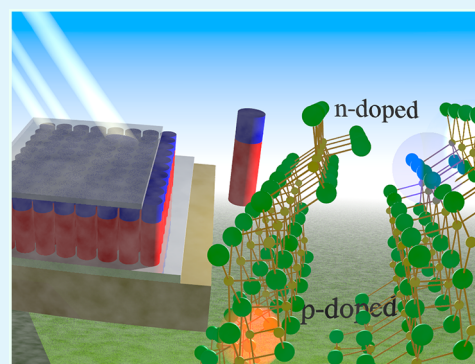
Read Online

ACCESS | Metrics & More | Article Recommendations | Supporting Information

ABSTRACT: Herein, we report a thorough investigation on Sb$_2$Se$_3$, a promising absorber material for photovoltaic applications, using state of the art quantum methods to understand the impact of defects on its electrical properties. The results show that despite a rather small stability domain, Sb$_2$Se$_3$ is easy to synthesize because there is no other possible stable competing binary phase in the Sb/Se system. Our calculations prove that formation of intrinsic n-type defects is unlikely, because Sb vacancies restrain the Fermi level from reaching the CBM vicinity. In contrast, intrinsic p-type semiconductor behavior is expected because of the Sb$_{Se}$ antisite defects. Doping is a commonly used technique to impact the charge carrier concentration as well as the charge carrier nature. In that context, several extrinsic defects were considered, based on tin and copper to enhance the native p-typeness, and halogenides (Cl, Br, I) to induce n-type doping in Sb$_2$Se$_3$. Our results tend to prove that Sb$_2$Se$_3$:Cu(p)/Sb$_2$Se$_3$:I(n) might be a viable homojunction for photovoltaic devices.

KEYWORDS: Sb$_2$Se$_3$, DFT, point defects, photovoltaics, chalcogenides, absorber, modeling

1. INTRODUCTION

The need for exploration of sustainable clean energies has become a global consensus because of the depletion of fossil fuels and increasing concerns of environmental protections.[1] Nowadays, the most commercially competitive technology among thin-film photovoltaics (PV) is CdTe because of its high device efficiency in relation to its excellent optoelectronic properties,[2,3] and the relatively low cost of its production. CIGS-based photovoltaic cells and modules offer higher performances but suffer from the scarcity of gallium and indium and lesser deposition rate due to the complexity of the absorber composition and its inherent versatility. Sb$_2$Se$_3$, with earth-abundant constituents, emerged recently as a very promising nontoxic alternative to CdTe and CIGS PV. Indeed, Sb$_2$Se$_3$-based solar cells received these past few years a strong incentive that led to a continuous and impressive increase in the conversion efficiency, η. Actually, this latter shifted successively from 2.6 and 2.7% in 2014;[4,5] to 4.7% in 2015;[6] 5.6, 5.8, and 6.5% in 2017;[7−9] and 7.04% in 2018,[10] to reach finally 9.21% in 2019.[11] This very fast improvement is very encouraging and suggests that characteristics may still progress in the near future, in particular through a better control of interfaces and a mastering of charge carrier concentrations. To do so, the understanding of the impact of defects on transport properties is crucial, as they play a pivotal role on thin-film solar cell performances, as well as grain boundaries and interfaces, two subjects not discussed herein.

Naturally, antimony selenide (Sb$_2$Se$_3$) is a p-type semi-conductor with a one-dimensional crystal character.[12] The mobility of minority carriers (n) is decent for the target application ($\sim$10 cm^2 V^{-1} s^{-1}) as well as carrier lifetime ($\sim$60 ns according to transient absorption measurements).[13] More-over, Sb$_2$Se$_3$ displays all the requisites to be an excellent PV absorber, i.e., a high absorption coefficient ($>1 \times 10^5$ cm^{-1})[4] and an optical gap of ca. 1.2 eV, i.e., a value next to the optimal one for a single junction solar cell).[14] In addition, theoretical calculations[15,16] allude that Sb$_2$Se$_3$ can be regarded as a promising candidate for achieving a power conversion efficiency (PCE) as high as 20%. A recent investigation concerning the point defects of Sb$_2$Se$_3$ demonstrated the role of antimony vacancies as a pinner of the Fermi level. In this study, the authors used screened hybrid functional HSE of which they tweaked the share of Hartree−Fock exchange at short-range (α parameter).[17] The density functional theory was used together with many body approaches to investigate the impact of both intrinsic and extrinsic defects on the characteristics of Sb$_2$Se$_3$. Indeed, our simulation focuses on
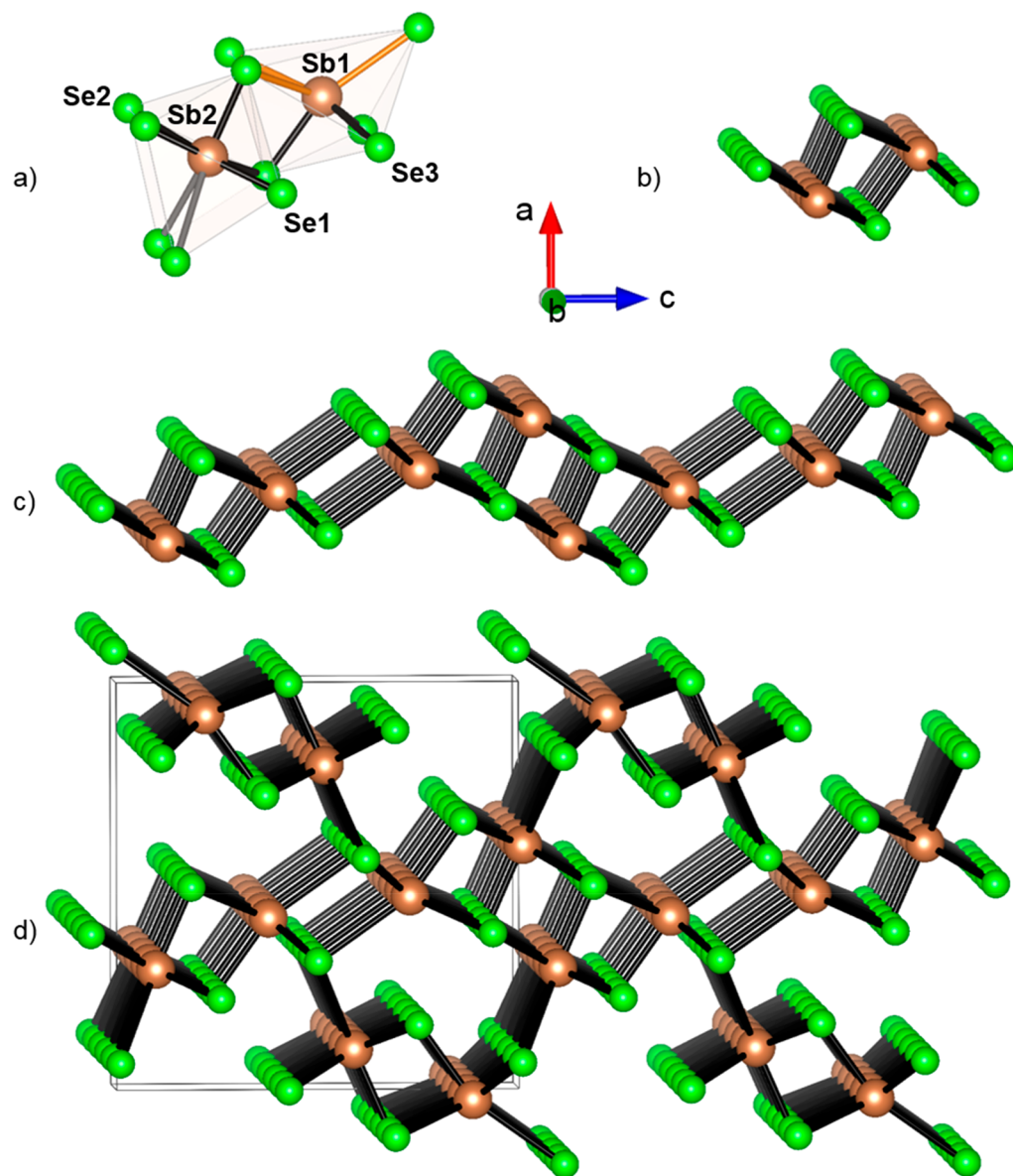
Figure 1. Sb_2Se_3 crystallographic structure (SG: *Pnma*) (a) $[Sb(1)Se_6]$ and $[Sb(2)Se_7]$ polyhedra, bonds are colored according to their length (<3.1 Å, black; <3.3 Å, orange; <3.5 Å, gray);[26] (b) infinite $^1/_\infty[Sb_4Se_6]$ ribbons running along the *b*-axis; (c) condensation of $^1/_\infty[Sb_4Se_6]$ ribbons along the *c*-axis to define $^2/_\infty[Sb_2Se_3]$ layers running in the (100) planes when considering Sb–Se bond lengths comprised between 3.1 and 3.3 Å; (d) condensation of $^2/_\infty[Sb_2Se_3]$ layers along the *a*-axis to define a tridimensional array. The conventional cell borders are drawn in black.

point defects to create p-type and n-type semiconductors with high hole or electrons concentrations.

2. COMPUTATIONAL DETAILS

DFT computations using semilocal PBE functional[18] on a 1 × 3 × 1 supercell containing 60 atoms were performed within the projector augmented-wave (PAW) scheme as implemented in the VASP software (Vienna Ab-initio Simulation Package),[19−21] similarly to Liu et al. and Savory and Scanlon.[8,22] The energy cutoff for plane waves was set at 350 eV. The first Brillouin zone was sampled with a 4 × 4 × 4 mesh following a Monkhorst−Pack scheme for structural relaxation and 5 × 5 × 5 mesh for accurate total energy calculations, respectively.[25]

We compare different methodologies to account for the dispersion forces, including or not Becke-Johnson damping factor (see Table S1).[23] Without any dispersion, PBE catastrophically overestimates the *a* parameter (+8.0%),

highlighting the need for dispersion corrections (only ±1% for *b* and *c*). GD3 scheme performs much better with a deviation on cell parameters with respect to experiment of ±2%. GD3-BJ overcorrects dispersion effects and leads to a systematic underestimation of cell parameters. This is particularly visible on the volume of the cell. Therefore, all the data discussed herein are with the PBE + GD3 scheme.[23,24]

Refined lattice parameters (see the Supporting Information) turn out to be in very good agreement with respect to available experimental data. Indeed, the optimized *a*, *b*, and *c* parameters are computed at 12.015, 4.019, and 11.465 Å, respectively. They match the experimental ones obtained via X-ray diffraction, i.e., 11.805, 3.988, and 11.662 Å, for *a*, *b*, and *c*, respectively (SG: *Pnma*).[26]

Defect formation enthalpies have been calculated using the supercell approach, as given in eq 1.
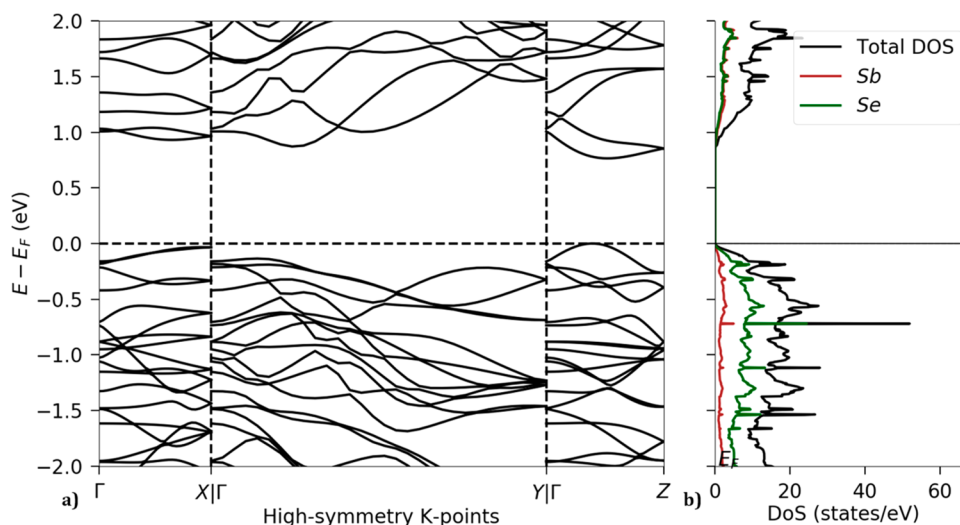
Figure 2. (a) Electronic band structure and (b) densities of states of Sb_2Se_3 calculated with PBE-GD3. Γ (0,0,0), X (0.5,0,0), Y (0,0.5,0), Z (0,0,0.5).
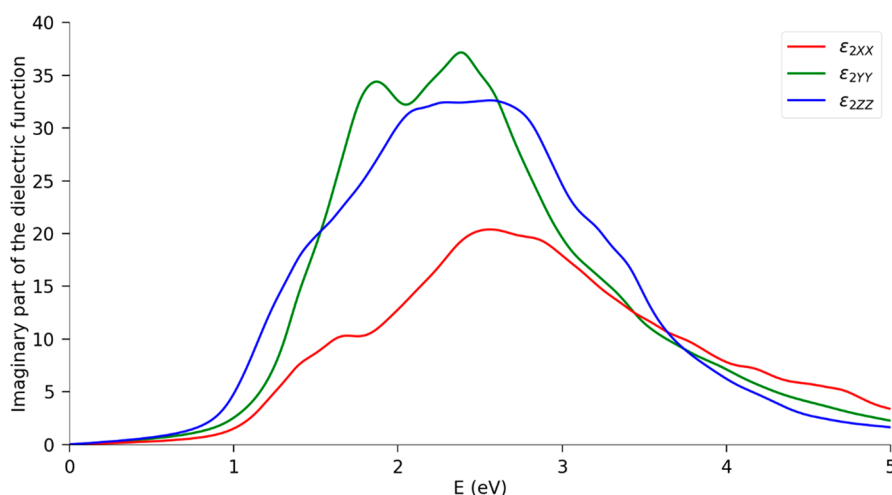

Figure 3. Imaginary part of the dielectric function of Sb_2Se_3 calculated with PBE functional.

$$\Delta H_{form}^{D,q}(\mu_{E_F}) = (E_{D,q} - E_H) + \sum_i n_i \mu_i + q_{E_F} + E_{corr} \tag{1}$$

$$\epsilon_{q1,q2} = -\frac{\Delta H^{D,q_1}(0) - \Delta H^{D,q_2}(0)}{q_1 - q_2} \tag{2}$$

where $E_{D,q}$ and E_H are the total energies of the faulted and perfect cell respectively, μ_i is the chemical potential of the ith chemical species, μ_{EF} is the chemical potential of the electrons (Fermi level), and E_{corr} are the various corrections included to account for the limitations of the supercell model. Band edges positions were corrected based on the results of a GW calculation. An electrostatic potential alignment correction was taken into account. Spurious electrostatic interactions between charged defects and their periodic images were dealt with using Makov–Payne style correction. Moss-Burstein type band-filling effect and perturbed host states correction were taken into account as well. In the dilute limit, the variation in volume due to the creation of a defect is negligible so that the calculated defect formation energy reasonably approximates the formation enthalpy. All defect post-treatments were executed with the PyDEF code.[27,28] The energy state at which the charge of a given defect is changing, i.e., the transition state, was determined by plotting enthalpy vs. Fermi level (μ_{EF}) position. It can be expressed as

It should be noted that we have tested the consistency of our results by using a larger supercell, namely $2 \times 3 \times 2$ supercell. It leads to no significant changes as evidenced in Table S2.

The defect concentration, $n_{D,q}(E_F)$ of a defect D in charge state q, can be approximated using a Boltzmann distribution depending on the position of the Fermi level during synthesis E_F, as expressed in

$$n_{D,q}(E_F) \approx N \exp\left(\frac{-\Delta H_{form}^{D,q}(E_F)}{k_B T}\right) \tag{3}$$

where k_B is the Boltzmann constant, N is the number of sites available to the defect divided by the cell volume, and T is the temperature of the synthesis. The entropic contribution to the Gibbs' free energy is considered negligible with respect to the enthalpic terms. The material is globally charge neutral, which sets the value of the Fermi energy so that to compensate the charges of the carriers (holes and electrons) with the ones of the defects. Numerically, this translates as the following
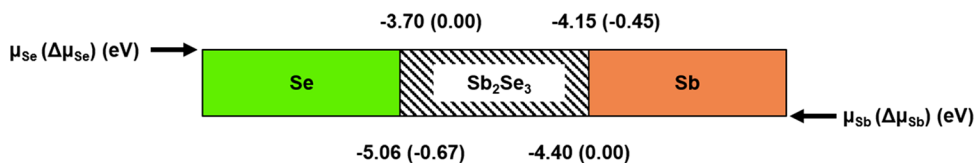
Figure 4. Stability domain of Sb_2Se_3 vs μ_{Sb} (bottom axis) and μ_{Se} (top axis). The deviation of chemical potential from the reference most thermodynamically stable phase is indicated in brackets.
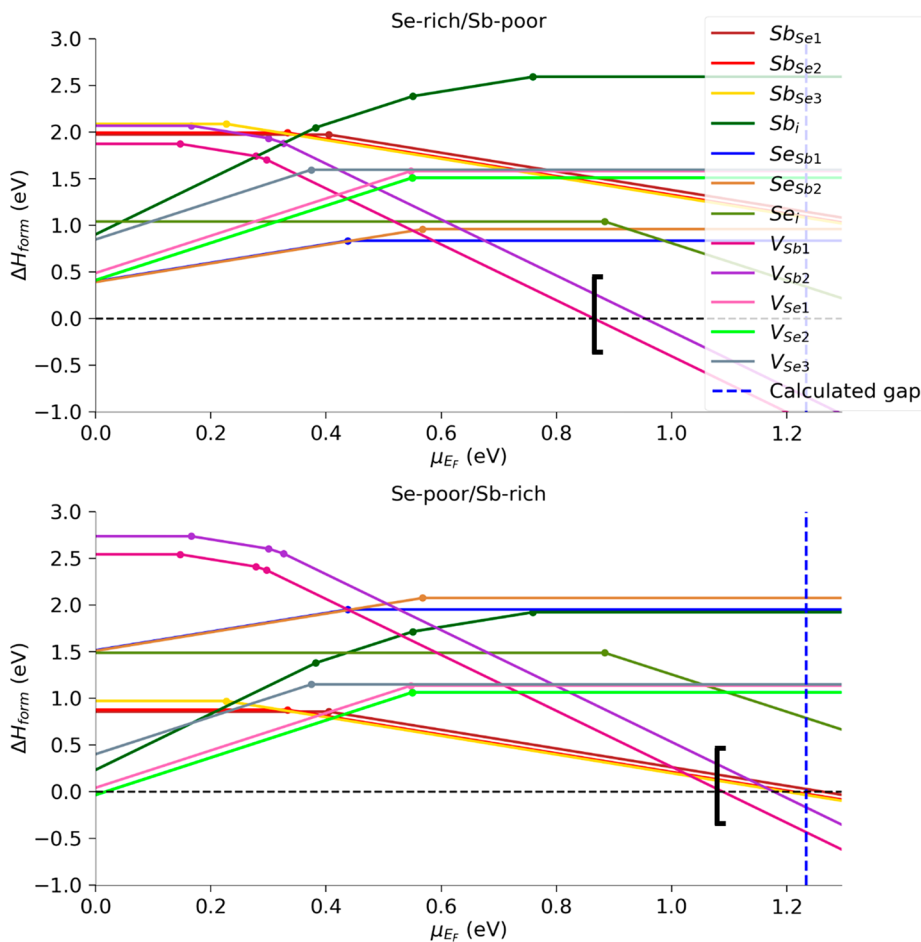

Figure 5. Formation enthalpies of the vacancies vs Fermi level in Se-rich (top) and Se-poor (bottom) conditions. Each line corresponds to the charge (encapsulated) exhibiting the lowest formation enthalpy. Points mark transition levels. Brackets highlight the dopability limit.

equation, whose resolution leads to the determination of the Fermi level:

$$-n_e(E_F) + n_h(E_F) + \sum_D q_D n_{D,q_D}(E_F) = 0 \tag{4}$$

Here, $n_e(E_F)$ and $n_h(E_F)$ are the concentrations of free electrons and holes, respectively, for a Fermi energy at a given temperature. They are given by the following equations:

$$n_e(E_F) = \int_{E_C}^{+\infty} g_e(\mu) f_{FD}(\mu - E_F) d\mu \tag{5}$$

and

$$n_h(E_F) = \int_{-\infty}^{E_V} g_h(\mu)(1 - f_{FD}(\mu - E_F)) d\mu \tag{6}$$

where $f_{FD}(\mu - E_F)$ is the Fermi–Dirac function:

$$f_{FD}(\mu - E_F) = \frac{1}{1 + \exp\left(\frac{\mu - E_F}{k_B T}\right)} \tag{7}$$

and $g_e(\mu)$ and $g_h(\mu)$ are the density of states of respectively electrons and holes for a 3D solid:

$$g_{e,h}(\mu) = \frac{1}{4\pi^2}\left(\frac{2m_{e,h}^*}{\hbar^2}\right)^{3/2} \sqrt{\mu} \tag{8}$$

3. RESULTS AND DISCUSSIONS

3.1. Perfect Cell. Sb_2Se_3 crystallizes in the stibnite structure type (*Pnma*, SG No. 62). Two and three types of antimony and selenium sites are crystallographically distinguishable, respectively (all of them are located at a 4*c* Wyckoff position). [Sb(1)Se$_6$] and [Sb(2)Se$_7$] polyhedra can be viewed as strongly distorted octahedra (three short ($d_{Sb-Se} < 3.1$ Å) and three medium (3.1 Å $< d_{Sb-Se} < 3.3$ Å) Sb−Se distances),
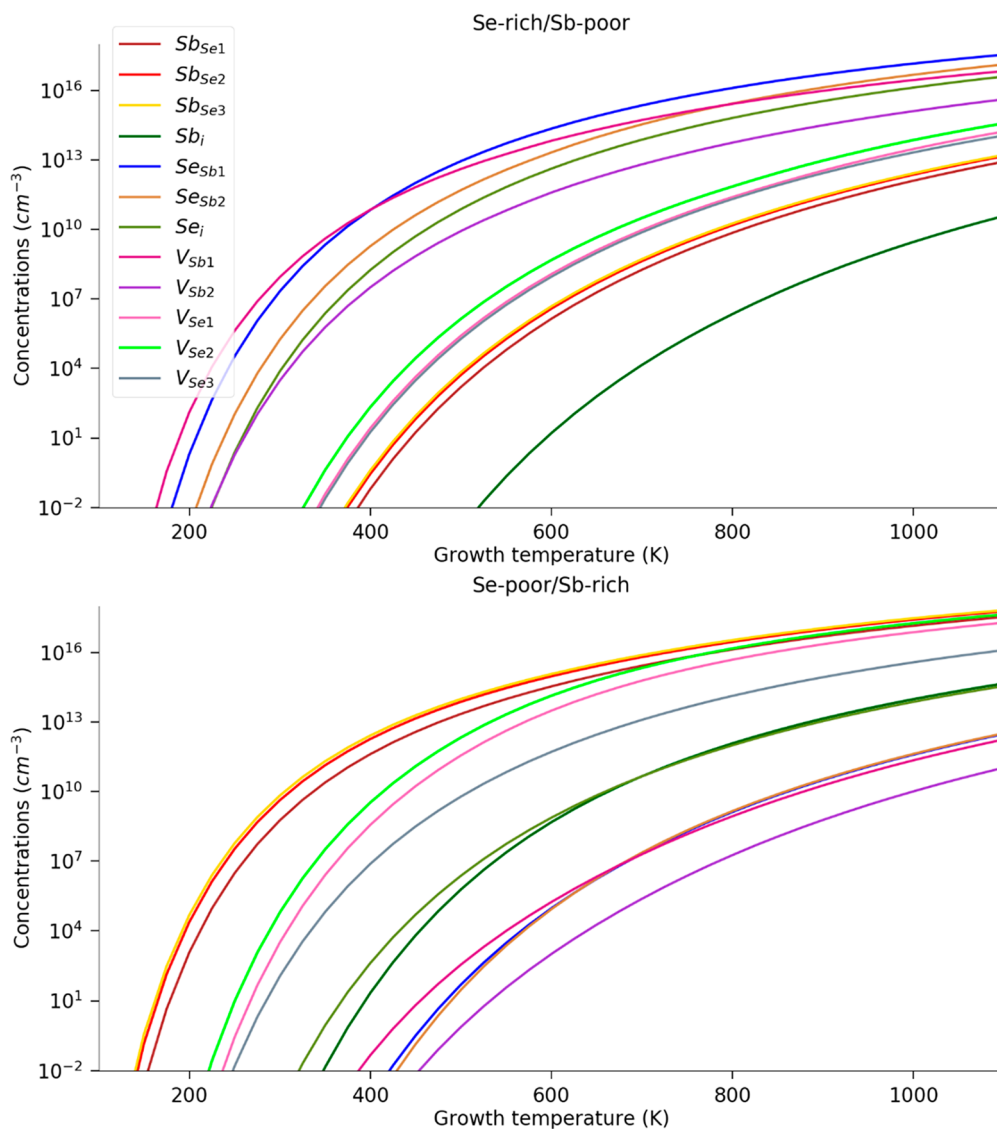
Figure 6. Intrinsic defect concentrations in Sb_2Se_3 with respect to synthesis conditions.
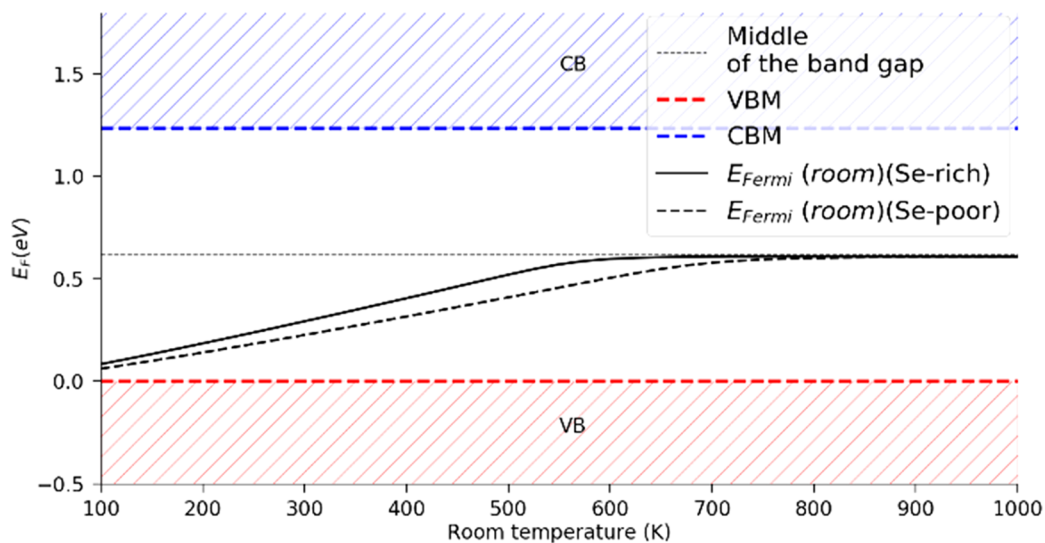

Figure 7. Simulated Fermi level as a function of operating temperature for a model synthesis temperature of 550 K in different growth conditions (Se-rich/Sb-poor, solid line; Se-poor/Sb-rich, dashed line).

Table 1. Comparison between Reference Chemical Potential and Maximum Chemical Potential Value for Sb_2Se_3 Doping Obtained by Considering the Stability Domain of the Sb_2Se_3 Host in the Sb−Se−X Ternary System

dopant	μ_0 (eV)	phase	$\mu_{max}^{Se\text{-}rich}$	phase	$\mu_{max}^{Se\text{-}poor}$	phase
Sn	−3.98	β Sn ($I4_1/amd$)	−5.12	$SnSe_2$	−4.53	SeSn
Cu	−4.24	fcc Cu($Fm\overline{3}m$)	−4.50	Cu_3SbSe_4	−4.21	$CuSbSe_2$
Cl	−1.79	$Cl_{2(g)}$	−2.87	$SbCl_3$	−3.10	$SbCl_3$
Br	[a]	$Br_{(l)}$	−2.48	SbSeBr	−2.72	SbSeBr
I	−1.78	$I_{2(s)}$ ($Cmca$)	−2.06	SbSeI	−2.30	SbSeI

[a]The reference thermodynamic state for Br is liquid bromine, which was not calculated herein.
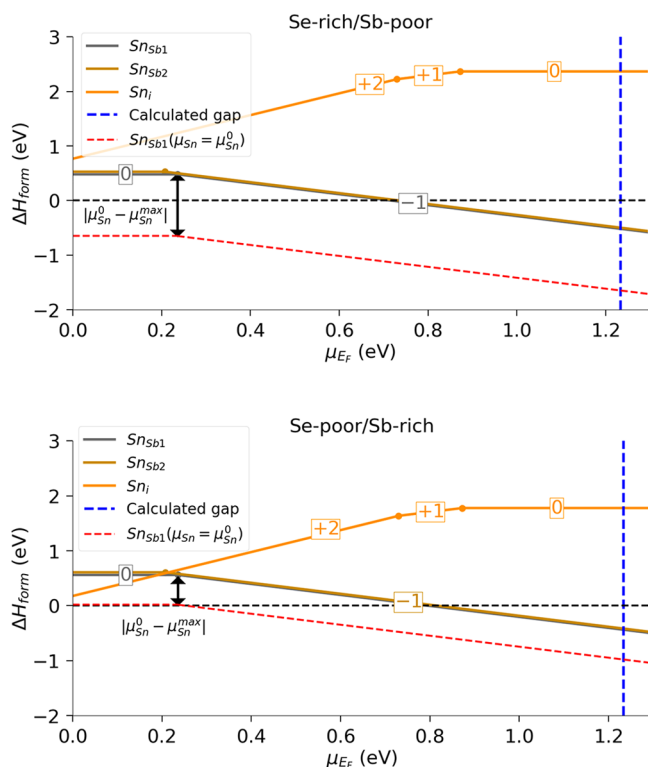

Figure 8. Sn-extrinsic point defect formation enthalpy vs Fermi level in Se-rich (top) and Se-poor (bottom) conditions. Each line corresponds to the charge (encapsulated) exhibiting the lowest formation enthalpy. Points mark transition levels. The dashed red line corresponds to the formation enthalpy of Sn_{Sb1} calculated using the potential for tin in its elemental form to illustrate how this choice favors the decomposition of the host (negative defect formation enthalpy).

and bicapped square pyramids (five short ($d_{Sb−Se} < 3.1$ Å) and two long ($d_{Sb−Se} > 3.3$ Å) Sb−Se distances) (Figure 1a). To some respect, if only short Sb−Se interactions are taken into account (strong covalent bonds, $\nu_{Sb\_Se} > 0.24$ (ν_{Sb_Se} = bond valence between Sb and Se atoms),[29] Sb_2Se_3 can be regarded as $^1/_\infty[Sb_4Se_6]$ infinite ribbons running along the b-axis of the orthorhombic cell (Figure 1b). If one considers medium Sb−Se distances (medium covalent bonds, $0.14 < \nu_{Sb\_Se} < 0.24$), these ribbons condense along the c direction to define $^2/_\infty[Sb_2Se_3]$ infinite layers lying in the (100) planes (Figure 1c). These planes interact altogether via very weak interactions (3.3 Å $< d_{Sb−Se} < 3.6$ Å, $0.06 < \nu_{Sb\_Se} < 0.14$) along the a-axis to generate a tridimensional array (Figure 1d). Let us notice that Sb_2Se_3 is sometimes also described in the $Pbnm$ unconventional space group, which may be a severe source of misunderstanding in discussion of physical properties in the direct and reciprocal spaces.[11]

Next, we investigate the electronic structure of the ideal cell, as shown in Figure 2 to determine the direction in which the photogenerated charge carriers flow in order to favor charge extraction in the device. The valence band maximum (VBM) is reached between Γ and Z (0,0,0.5) in reciprocal space, along the c^* axis. The bandgap is direct and calculated at 0.77 eV with PBE-GD3 functional. As expected in GGA, the gap is underestimated with respect to the experimental optical value of ~1.2 eV.[30,31]

From the analysis of the atomic structure, the highest dispersion is along the Γ-Y segment in reciprocal space, and then along the Γ-Z segment. Clearly, it corresponds to the directions defining the $^2/_\infty[Sb_2Se_3]$ layers in direct space. The dispersion of the bands is smaller along the Γ-X segment, which corresponds to the direction perpendicular to the $^2/_\infty[Sb_2Se_3]$ layers, i.e. a direction where Sb−Se bonds are weak. The highest occupied electronic band along this segment does not reach the Fermi level (the band lies a few meV below E_F even at the X high-symmetry point). Thus, based on the analysis of the band structure, free holes are counterintuitively more likely to propagate along the c axis, i.e., the in-plane direction perpendicular to the chains. A similar conclusion would prevail for free electrons after examination of the dispersion of the conduction band.

The projection of the density of states (DOS) on the atomic orbitals show that the valence band mainly comes from the selenium orbitals, whereas the conduction band has a mixed antimony and chalcogenide character. It is important to reproduce accurately the bandgap for the following point defect study. To overcome the bandgap problem of GGA, we performed a GW0 calculation on top of the PBE-GD3 geometry, yielding a gap value of 1.24 eV, in excellent agreement with the experimental gap. We have used this value to correct the bandgap for all faulted cell calculations (vide infra).

In thin films, one usually observes Sb_2Se_3 rods growing preferentially along the chain direction.[32,33] This encourages us to assess the propensity of this anisotropic material to absorb light along the different spatial directions. In order to do so, the imaginary part of the dielectric function is presented in Figure 3.

Plots of the dielectric function along a, b, and c demonstrate that absorption along the b and c directions is strongly favored compared to the a one. Moreover, the band analysis (vide supra) shows that the highest carrier mobility will be obtained following the c direction. Consequently, one can deduce that Sb_2Se_3 crystal should be grown along the c direction in order to maximize both the absorption of the light and the extraction of the photogenerated charge carriers. However, this may require a strong deposition process tuning to overcome the natural orientation along the b axis.
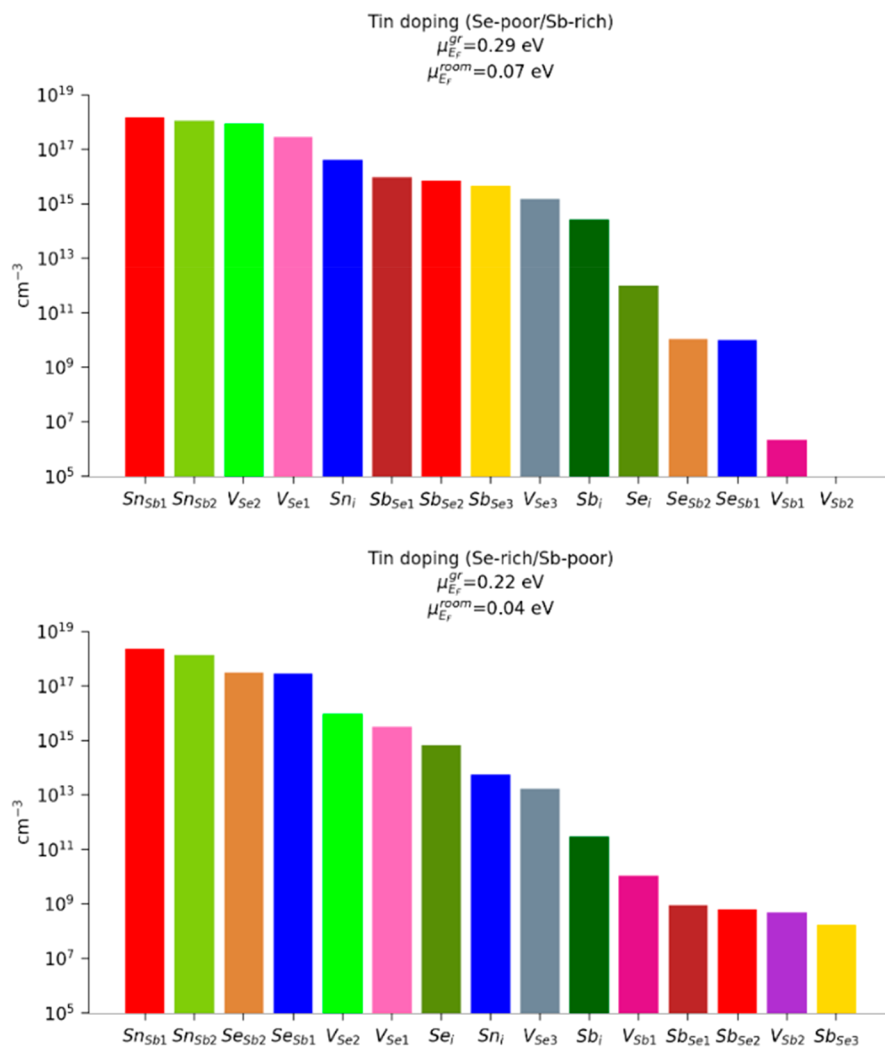
Figure 9. Estimated defect concentrations for tin doping at T_{growth}= 800 K in Se-poor (top) and Se-rich (bottom) conditions, together with intrinsic defects.

The absorption of incoming light will generate free electron−hole pairs harvested in the form of an electrical current. Fast and efficient design of devices requires the optimization of the electrical conductivity of the material. In order to rationalize the fair p-type conduction of undoped Sb_2Se_3,[13] the intrinsic point defects of the material, namely, vacancies, self-interstitials, and antisites, were investigated.

3.2. Intrinsic Defects to Determine the Origin of the Electronic Properties. In that context, we first need to set the values of the chemical potentials to properly account for the experimental synthesis conditions. As aforementioned, Sb_2Se_3 is the only binary compound of the Sb−Se system, so that the limits of its stability domain are set by the reference phases of each element i.e. elemental Se and Sb in their hexagonal and rhombohedral forms, respectively, as shown in Figure 4. Two limit cases have to be envisioned, i.e., the Se-rich/Sb-poor conditions at the frontier with the domain of the selenium (where the potential of Sb is fixed by rhombohedral antimony) and the Se-poor/Sb-rich ones on the Sb side (where the potential of Se is fixed by hexagonal selenium).

The formation enthalpy of all five possible vacancies in Sb_2Se_3 (V_{Sb1}, V_{Sb2}, V_{Se1}, V_{Se2}, V_{Se3}) are summarized in Figure 5. The transition levels are in total agreement with computations performed using hybrid functional HSE06-D3 performed by

Savory and Scanlon, which fully validates our methodology.[22] Huang et al. also showed that the transition level positions are not affected by going from HSE to PBE.[17] Here, both antimony vacancies V_{Sb1} and V_{Sb2} present an acceptor character with a transition level 0/−1 0.15 eV above the VBM. In both synthesis conditions, they possess a quite high enthalpy of formation, which suggests that their concentration in the material will not be important (vide infra). Moreover, and most importantly, the selenium vacancies are lower than Sb ones in enthalpy at low μ_{EF}, especially for Se-poor/Sb-rich synthesis conditions, and are (very deep) donor defects which will capture the holes produced by the formation of V_{Sb} ("hole killer" defects). Thus, the observed p-type conductivity cannot result from V_{Sb}. The formation enthalpy of V_{Sb} becomes negative as the Fermi level approaches the CBM. If the Fermi level enters this region, these vacancies would be so easy to form that they would drive the ongoing synthesis off-stoichiometry to finally lead to another phase (according to the stability domain, demixing into elemental Sb and Se). Thus, the zero enthalpy crossing of V_{Sb} marks the limit of a forbidden domain for the Fermi level (n-type dopability limit). In other words, μ_{EF} cannot explore the region close to the CBM, so even doping cannot lead to n-type conductivity in such conditions. The dopability limit is deep in the gap for the
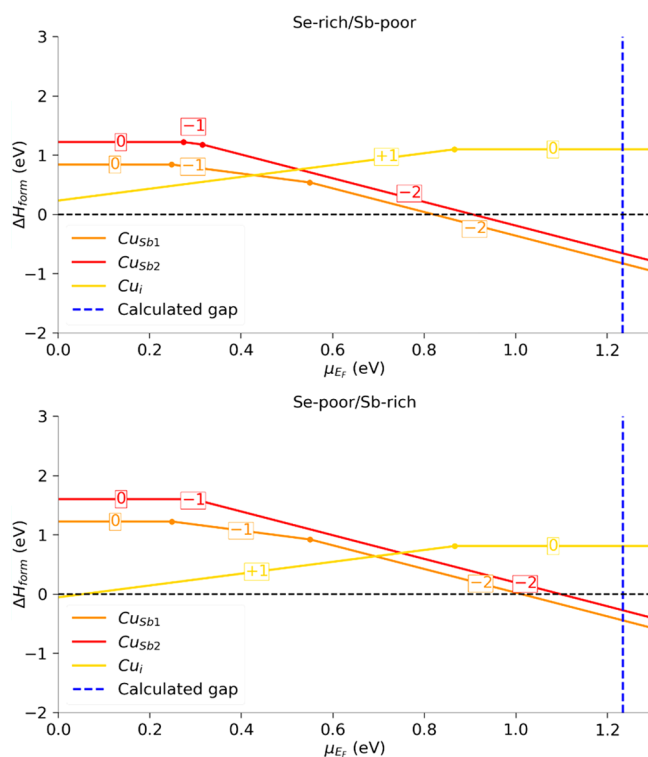
Figure 10. Cu-extrinsic point defect formation enthalpy vs Fermi level in Se-rich (top) and Se-poor (bottom) conditions. Each line corresponds to the charge (encapsulated) exhibiting the lowest formation enthalpy. Points mark transition levels.

Se-rich/Sb-poor atmosphere (0.25 eV below the CBM) and tolerable for the Se-poor/Sb-rich limit case (0.09 eV below the CBM), so the excess in selenium is detrimental to n-type doping.

We then investigate the formation of self-interstitials. To locate the possible interstitial sites, we use the plots of isosurfaces of the charge density as drawn in Figure S1.

Both Se_i and Sb_i defects are deep defects and will therefore barely affect the electronic conductivity of the material. The formation enthalpy of the selenium interstitial is lower than that of the antimony one, and inferior to 2 eV. Additionally, steric and charge effects may play a role, the anion being smaller than the cation.

None of the defects investigated so far give a satisfactory explanation for the natural p-type conductivity of the undoped material. Antimony has the peculiar property to be able to show both cationic, Sb^{3+} (as in Sb_2Se_3), and anionic, Sb^{3-} (as in AlSb), characters by, respectively, emptying and filling the 5p electronic orbital.

Thus, the formation of an antisite, i.e. the substitution of Se by Sb and vice versa, is deemed possible. Regardless of the synthesis conditions, the enthalpies are under 2 eV, which supports our claim that antisites can be abundant in this material. Se_{Sb} antisites are very deep donor defects ($\mu_{EF} \approx 0.70$ eV under CBM) which will not affect the electronic properties. Sb_{Se} antisites are acceptor defects with a low formation enthalpy (<2 eV). Sb_{Se1} and Sb_{Se2} antisites exhibit almost the same behavior with a transition level $0/-1$ located 0.33 and 0.40 eV, respectively, above the VBM. They both occupy a corner of the square-based pyramid of Sb_2 but the Sb_2-Sb_{Se1} and Sb_2-Sb_{Se2} bond lengths differ. For the Sb_{Se3} antisite, Sb atom is bonded to Sb_1 and the associated defect has a

shallower transition level (0.23 eV). Its formation enthalpy is lower than that of the hole killers V_{Se}. It is thus the shallowest intrinsic acceptor, even though the position of its transition level is not in the optimal region situated under 0.1 eV (a few k_BT) above the VBM. This clearly demonstrates that the intrinsic p-type conductivity of Sb_2Se_3 is likely due to the formation of Sb_{Se3} antisites. This result is fully consistent with previous literature performed with the HSE06 hybrid functional,[22] which fully validates the use of PBE-D3 to describe the defect physics in this material.

Now that we have determined the formation enthalpies and electronic properties of a wide range of intrinsic defects, we can estimate their concentration at a given synthesis temperature. Indeed, the material is globally charge neutral, so that the electrostatic charges of the different defects and charge carriers must sum up to zero. This can be written as eq 4. n_e is the concentration of electrons, n_h of holes, derived from the density of states, and n_D, q_D the concentration of defect. As the concentrations are functions of the Fermi level, solving it through a standard root-finding algorithm method yields the Fermi level during crystal growth at a given growth temperature (T_{growth}).

The defect concentration can then be approximated by a Boltzmann distribution, as expressed in eq 3. Effective masses of electrons and holes were estimated from a parabolic fitting of the band summits of the conduction and valence bands, respectively ($m_{e*} = 0.365 m_e$ and $m_{h*} = 0.316 m_e$).

The obtained defect concentrations are shown in Figure 6. For a material synthesized at 550 K, which corresponds to a realistic temperature in a physical vapor deposition of a Sb_2Se_3 thin film, the most prevalent defect in Se-rich/Sb-poor conditions is the Se_{Sb1} antisite with a concentration of $\sim6 \times 10^{13}$ cm^{-3}. This defect exhibits only one transition level deep in the gap and is thus of weak interest with respect to the electrical properties. The second most important defect is V_{Sb1} up to $T_{growth} \approx 790$ K and Se_{Sb2} for higher synthesis temperatures. Regardless of the growth temperature, such material is expected not to display electrical properties sufficient for device application. In Se-poor/Sb-rich conditions for the same growth temperature of 550 K, the major defects are Sb_{Se2} and Sb_{Se3}, exhibiting a concentration of $\sim1 \times 10^{14}$ cm^{-3}. Sb_{Se3} is responsible for the p-type character of the material. Such concentrations are similar to those met in silicon, the base material for the electronic industry and therefore used in photovoltaics.[34] However, the transition level is a bit far from the VBM, possibly explaining the not-so-good observed electrical properties. Computed positive charge carrier (hole) concentrations (n_h) at room temperature are of 5.5×10^{13} cm^{-3} in Se-rich/Sb-poor atmosphere and 7.2×10^{14} cm^{-3} in Se-poor/Sb-rich.

Because of its fast cooling just after formation, the stoichiometry of the material at high temperature (e.g., ca. 550 K) can be considered as quenched at room temperature. Thus, all the defects created during the high-temperature process are frozen when the system cools down from growth to (device) operating temperature. Solving the charge neutrality equation at fixed defect concentrations then yields the Fermi level at operating temperature. The result is shown in Figure 7 for the two synthesis atmospheres and a growth temperature of 550 K. The behavior is typical of a p-type semiconductor: at low temperature, the Fermi level is pinned close to the VBM and when the operating temperature increases, the Fermi level moves toward the middle of the bandgap. At very high
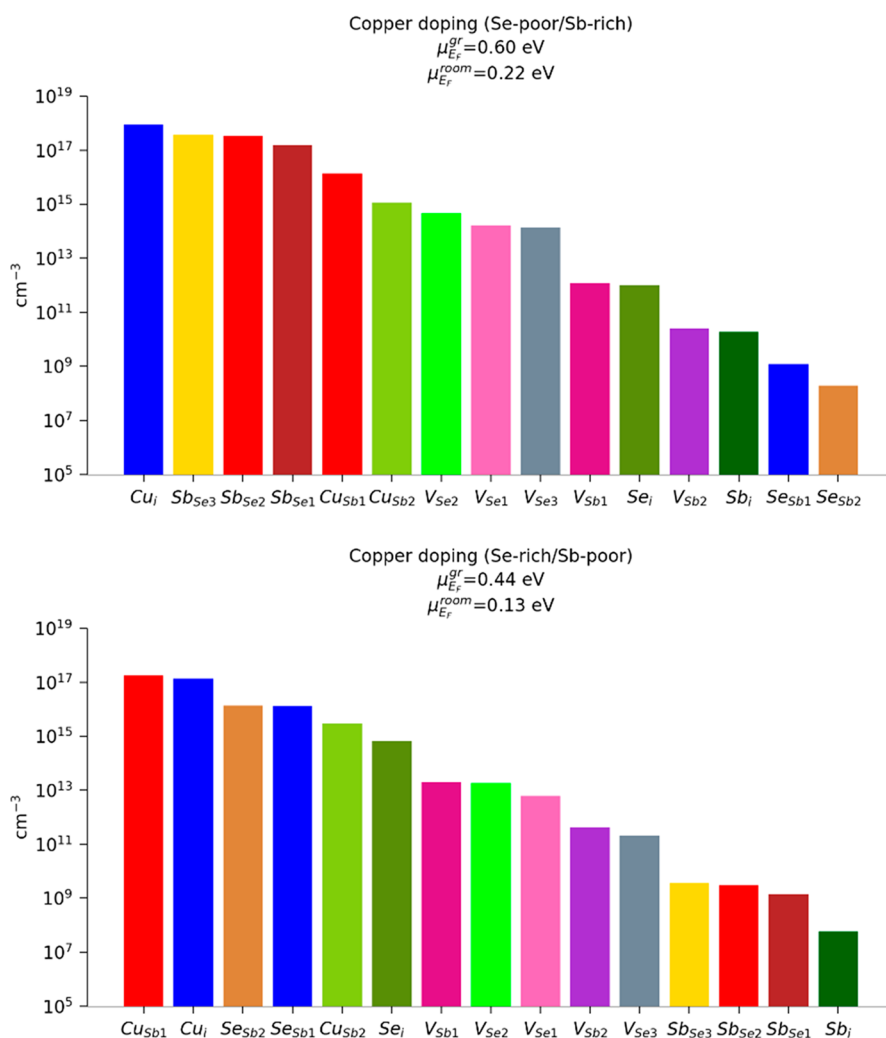
Figure 11. Estimated defect concentrations for Cu-doping at T_{growth} = 800 K in Se-poor (top) and Se-rich (bottom) conditions, together with intrinsic defects.

temperatures (see the Supporting Information), the simulation would follow the theoretical behavior $E_F = \frac{E_g}{2} + \frac{3}{4}k_B T \ln\left(\frac{m_h^*}{m_e^*}\right)$ (Figure S5) (these high temperatures are of course not reachable because of the natural instability of the material, but our calculations prove that our model matches semiconductor physics).

3.3. Sn Doping. The first dopant considered is tin, an earth-abundant and low-cost element, that was recently tried out experimentally.[35] Two types of defects must be considered, cationic substitution and interstitial. Substituting an antimony atom (Z = 51) with a tin atom (Z = 50) is expected to form an electronic hole, thus leading to p-type doping. At the opposite, a tin interstitial is expected to be a donor defect as it can release an electron by switching from neutral to positive states of charge. The chemical potential of the dopant is usually taken at the reference thermodynamical value. As we recently discussed,[36] this corresponds to synthesis conditions at the limit of formation of the reference thermodynamic compound, tin metal in tetragonal (β) form in this case. However, this does not reflect the synthesis conditions used to incorporate a dopant, i.e., a dilute point defect in the Sb_2Se_3 host lattice. Choosing the standard chemical potential value for the doping chemical species will strongly favor dopant-related defects

(here tin interstitials and substitutions), so much that they will exhibit a negative defect formation enthalpy, thus driving the formation of another phase.

Defining the chemical potential of the extrinsic dopant Sn thus requires taking into account all Sn-based phases participating in the ternary Sn−Sb−Se system, i.e., β-Sn, $SnSe_2$, and SnSe. We can then define the limits of the chemical potential of tin, μ_{Sn}, with β-Sn for the upper limit and $SnSe_2$ and SnSe in Se-rich and Se-poor atmospheres for the lower limit, respectively (Table 1). Figure 8 provides the evolution of the formation energy with respect to the Fermi level position in the bandgap for the defects involving Sn. For Sn_{Sb1}, the curve resulting from the use of the upper limit (β-Sn as reference) is shown (dashed red line). It shows a shift of 1.14 and 0.55 eV toward the lower energies for Se-rich and Se-poor conditions, respectively. In summary, by considering $SnSe_2$ and SnSe phases, positive defect formation enthalpies are obtained, which means that conditions suited for the doping of the Sb_2Se_3 host by tin are reachable. The depth of this maximum chemical potential value for tin to avoid the formation of an undesired phase gives us information about the amount of tin that should be included in order to not destabilize the material. Here, chemical potential values are quite deep (lower than −4 eV), which means that the Sn/Sb ratio should be low in order
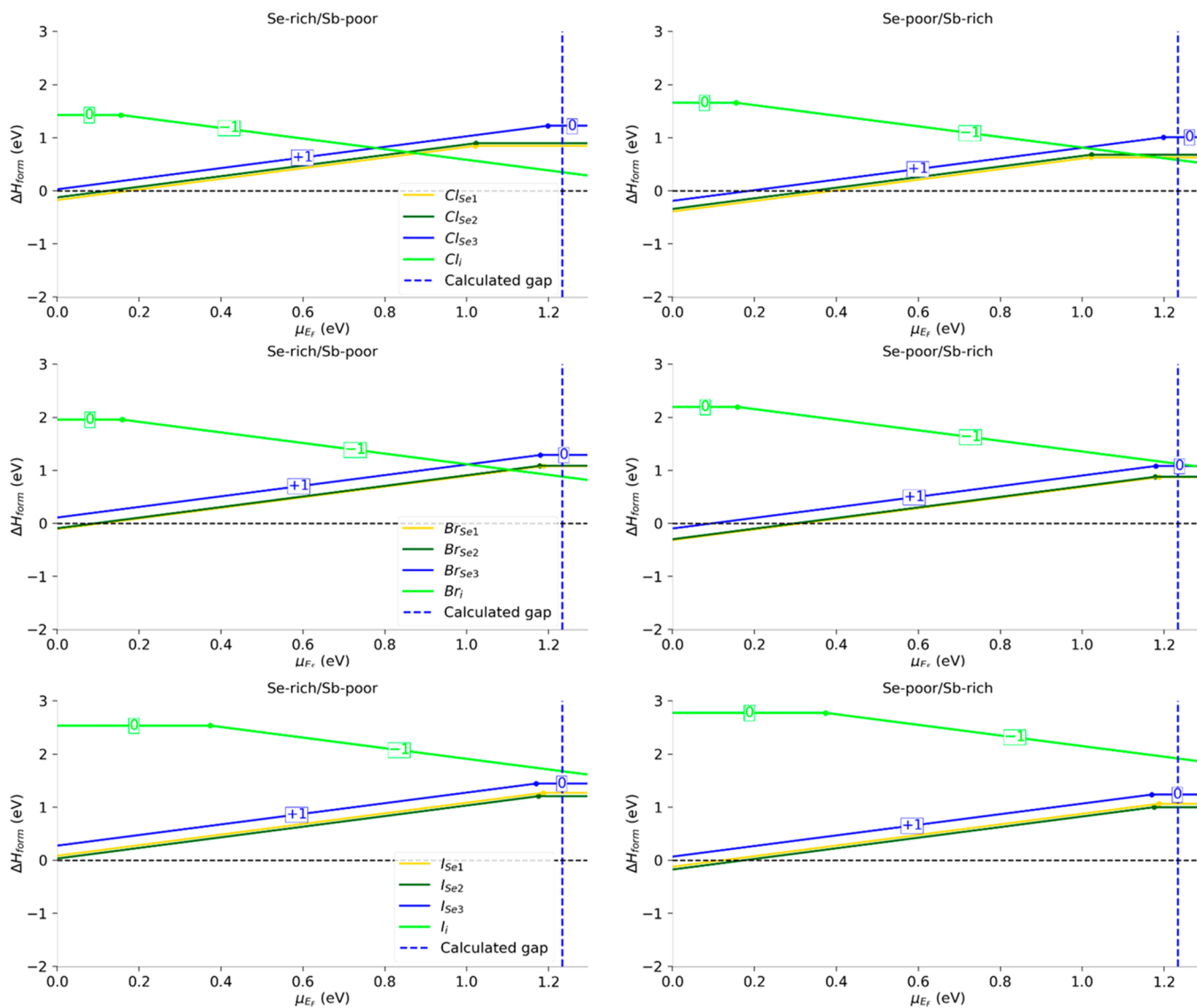
Figure 12. Cl/Br/I-extrinsic point defect formation enthalpy vs Fermi level. Each line corresponds to the charge (encapsulated) exhibiting the lowest formation enthalpy. Points mark transition levels.

not to destabilize the matrix. The $0/-1$ transition level is located ~0.24 eV above the VBM. It is roughly at the same position in the bandgap as the Sb_{Se_3} antisite responsible for the native (poor) p-type conductivity of the material.

Extrinsic defect concentrations can be deduced from eq 4. Of course, intrinsic defects are still present and must also all be taken into account. Because of the global charge balance, the addition of the external dopant affects the concentrations of the intrinsic defects as well. Additionally, considering the material quenched at growth temperature (800 K), freezing the lattice defects, the Fermi level at room temperature can be deduced from eq 4 with fixed concentrations obtained at growth temperature. All Fermi level values are summarized in Table S2. As the shape of the defect concentration vs. growth temperature curve has been discussed previously in Figure 6, we now only consider one representative growth temperature of 800 K. This temperature is close to the reported synthesis temperature (550 °C) by Huang and co-workers.[37] The resulting concentrations are shown in Figure 9. The main defect is the extrinsic substitution Sn_{Sb} as mentioned beforehand. The selenium vacancies in Se-poor conditions

and Se_{Sb} antisites in Se-rich conditions are also favored. They may act as recombination centers detrimental to the device and might hinder the gain in hole concentration.

In conclusion, the incorporation of tin will generate some additional holes in the material and thus will improve the p-type conductivity. However, due to the not optimal position of the transition level and the non-negligible formation of deep defects, the effect might not be as important as desired. Most importantly, the amount of tin which can be introduced inside the Sb_2Se_3 host without destabilizing the structure is small, $SnSe_2$ and $SnSe$ phases being highly thermodynamically stable in Se-rich/Sb-poor and Se-poor/Sb-rich, respectively. For the rest of the study, we will always take into account the phases in competition with Sb_2Se_3 in the ternary phase diagram to determine the chemical potential of the dopant. It has been indeed experimentally demonstrated that the substitution of Sb by Sn can improve the electrical conductivity of Sb_2Se_3.[35]

3.4. Cu Doping. Next, we investigate Cu doping. One should stress the nontoxicity and availability of copper as a dopant. Cu_3SbSe_4 and $CuSbSe_2$ phases limit the chemical potential of copper in Se-rich/Sb-poor and Se-poor/Sb-rich
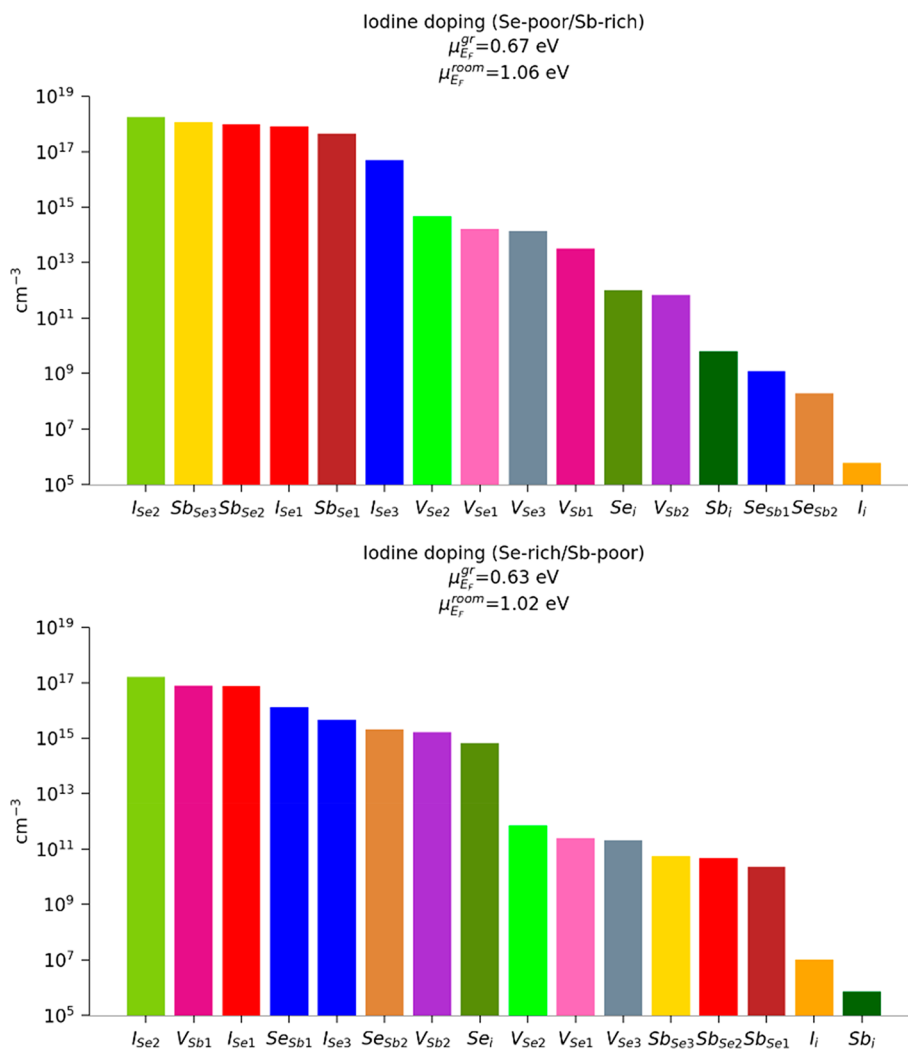
Figure 13. Estimated defect concentrations for iodine doping doping at T_{growth} = 800 K in Se-poor (top) and Se-rich (bottom) conditions, together with intrinsic defects.

atmospheres, respectively. The defect formation enthalpies are given in Figure 10. Let us start the analysis with the copper interstitials. The oxidation state of copper is expected to be + I in this material. Thus, Cu_i can be charged +1/0. This is a donor defect. It has a positive and not too high formation enthalpy ($\sim$1 eV); however, the transition level +1/0 is 0.37 eV below the CBM. Indeed, the level is unambiguously too deep to induce any n-type doping of the bulk material at room temperature, contrary to what was expected experimentally.[10] The n-type doping after $CuCl_2$ chemical bath proposed in this reference must be due to the Cl anion instead (vide infra). Next, we investigate the possible cationic substitutions in both Sb crystallographic sites. In Sb_2Se_3, the oxidation state of antimony is +III. Thus, the charge state of Cu_{Sb} varies between 0 and −2. This is an acceptor defect. In both synthesis conditions, the formation enthalpy of Cu_{Sb} is quite low (<1.7 eV). The formation enthalpy of Cu_{Sb1} is 0.39 eV lower than that of Cu_{Sb2}. The 0/−1 acceptor transition level is 0.25 eV above the VBM. One should recall that electronically active levels should be within a few $k_B T$ from the band extrema to be thermally activated, so this level is active but a bit too deep. This is compensated by a low formation enthalpy of the defect, which guarantees a high defect concentration. In short, each individual Cu_{Sb} defect has a fair but not so high probability of

generating a charge carrier (hole), but this is compensated by the important number of Cu_{Sb} defects in the doped material. Then, we calculate the defect concentrations for all copper-related defects along with the intrinsic defects of the material as presented in Figure 11. In Se-poor/Sb-rich synthesis conditions, the concentration of the (very poor) donor Cu_i is compensated by the formation of intrinsic antisite acceptors Sb_{Se} in comparable amount. Due to this competition, the Fermi level at room temperature (T = 300 K) lies 0.22 eV above the VBM, resulting in a slight p-type improvement. In Se-rich/Sb-poor atmosphere, the situation is similar to the competition between the extrinsic acceptor Cu_{Sb1} and extrinsic donor Cu_i, resulting in the Fermi level at room temperature pinned 0.13 eV above the VBM. These simulations tend to prove the stabilization of both Cu_i and Cu_{Sb} defects is possible, allowing a modest improvement of the p-type conductivity, especially in Se-rich/Sb-poor synthesis conditions.

3.5. Halogen Doping. So far, we have simulated p-type doping. In order to make a p−n homojunction, one also needs to grow n-type Sb_2Se_3. In that framework, we investigate the ability of halogen (Cl, Br, and I) extrinsic defects to produce such desired doping. The defect formation enthalpies are presented in Figure 12. Let us start with the lightest element of the three, chlorine.

The chemical potential is set by the limit of formation of $SbCl_3$ in both Se-poor and Se-rich limit conditions. The value is roughly 1 eV lower than the reference value, thus the amount of dopant which can be inserted is expected to be low. The formation enthalpy of chlorine interstitial is higher than that of the substitutions. The anionic substitutions are donor defects with transition levels located ~0.2 eV under the CBM for Cl_{Se1} and Cl_{Se2} and ~0.05 eV for Cl_{Se3}.

The latter is thus a very good donor defect. It exhibits a formation enthalpy of 1.25 eV so is expected to be quite abundant in the material. One should mention that the Cl_i acceptor defect crosses the lines of the donors (Cl_{Se1-3}) and, consequently, may prevent a good conductivity and potentially acts as an electron killer defect.

The cases of iodine and bromine are more promising than chlorine. In the case of bromine, the ternary phase SbSeBr limits the possible range of values for the chemical potential of Br. This time, the three Br_{Se} substitutions behave the same with a −1/0 transition level around 0.06 eV under the CBM. Consequently, all of them form very good donor defects. The interstitial is much higher in enthalpy and does not cross the lines of the substitutions in the band gap, although the enthalpy remains close to the interstitial near the CBM. Concerning I doping, the halogen chemical potential is set by SbSeI. The substitutions exhibit a −1/0 transition level roughly 0.10 eV below the CBM as for Br. In this case, the insertion of iodine in interstitial site is the most energy-consuming defect among the three halogens and never crosses the lines formed by the formation enthalpies of I_{Se1-3}. Consequently, this dopant seems to be the most favorable one.

In short, all three halogens considered are expected to significantly improve the electronic conductivity of the Sb_2Se_3 host. Our results provides a reasonable explanation for the n-type doping induced by $CuCl_2$ chemical bath treatment proposed in a previous work.[10] In terms of chemical potential, iodine has the highest allowed value of the three elements (the lowest in absolute value). This means that more iodine can be incorporated in the structure without destabilizing it as compared to bromine or chlorine. Based on this observation, only defect concentrations of defects involving iodine are presented in Figure 13 (see Figures S6 and S7 for chlorine and bromine).

For I as dopant, the Fermi level, both during crystal growth and during device use at room temperature, is pushed up toward the conduction band, undoubtedly the manifestation of n-type doping. Nevertheless, antimony-related p-type defects, i.e., Sb_{Se} antisite in Se-poor atmosphere and V_{Sb} in Se-rich atmosphere, still play an important role, being the second most concentrated defects after the donor I_{Se2} substitution. Experiments have been performed with iodine doping of Sb_2Se_3 and it has been demonstrated that high iodine content, up to 15 mol %, can be introduced in Sb_2Se_3 without phase separation, leading to a strong decrease of electric resistivity (8 orders of magnitude). Indeed, the obtained materials are stable n-type semiconductors.[38]

4. CONCLUSION

We conducted a thorough DFT investigation on the intrinsic defects of Sb_2Se_3 and their potential ability to induce p-type and n-type doping of the material. According to our calculations, V_{Se} act as hole killer defects, deteriorating the p-type conductivity of the material. V_{Sb} are too high in enthalpy to be responsible for the p-type and set the n-type dopability

limit. Thus, an excess in Selenium during synthesis would be detrimental to n-type doping. Thanks to the ability of Sb to act both as anion and cation, antisites in this material are fairly achievable defects. In particular, Sb_{Se} on the Se site bonded to the hexa-coordinated antimony (Se_3) exhibit a fair shallow transition level (0.23 eV) and a low formation enthalpy and is the best candidate to explain the (poor) intrinsic p-type conductivity of Sb_2Se_3. The study of tin and copper to achieve extrinsic p-type doping and halogens substitution for n-type doping of the absorber show that tin does not much improve the conductivity, while copper and the halogens provide good conductivities. Our results demonstrate that among the three investigated halogens, iodine seems the most promising dopant for the Sb_2Se_3 matrix. Consequently, $Sb_2Se_3:Cu(p)/Sb_2Se_3:I$-($n$) appears as a viable homojunction for photovoltaic devices.

◼ ASSOCIATED CONTENT

Ⓢ Supporting Information

The Supporting Information is available free of charge at https://pubs.acs.org/doi/10.1021/acsaem.9b02192.

Table S1, comparison of cell parameters computed with different dispersion corrections with respect to experimental structure; Table S2, comparison of defect formation enthalpy for two supercells; Table S3, calculated Fermi levels and free carrier concentrations at T_{growth} = 800 K and T_{room} = 300 K; Figure S1, charge density isosurfaces (yellow) in ideal Sb_2Se_3 conventional cell; Figure S2, formation enthalpies of the vacancies vs. Fermi level; Figure S3, formation enthalpies of Sb and Se interstitials vs Fermi level; Figure S4, formation enthalpies of antisites in Sb_2Se_3 vs. Fermi level; Figure S5, simulated Fermi level as a function of operating temperature for a model synthesis temperature of 550 K in Se-rich/Sb-poor synthesis conditions; Figure S6, estimated defect concentrations for chlorine doping at T_{growth} = 800 K; Figure S7, estimated defect concentrations for bromine doping at T_{growth} = 800 K (PDF)

◼ AUTHOR INFORMATION

Corresponding Authors

Camille Latouche − *Institut des Matériaux Jean Rouxel (IMN), Université de Nantes, CNRS, Nantes 44322, France;* ⓞ orcid.org/0000-0002-3541-3417; Email: camille.latouche@univ-nantes.fr

Xavier Rocquefelte − *Institut des Sciences Chimiques de Rennes UMR 6226, Université de Rennes 1, Rennes 35042, France;* ⓞ orcid.org/0000-0003-0191-2354; Email: xavier.rocquefelte@univ-rennes1.fr

Authors

Adrien Stoliaroff − *Institut des Matériaux Jean Rouxel (IMN), Université de Nantes, CNRS, Nantes 44322, France*

Alicia Lecomte − *Institut des Sciences Chimiques de Rennes UMR 6226, Université de Rennes 1, Rennes 35042, France*

Oleg Rubel − *Department of Materials Science and Engineering, McMaster University, Ontario L8S 4L8, Canada*

Stéphane Jobic − *Institut des Matériaux Jean Rouxel (IMN), Université de Nantes, CNRS, Nantes 44322, France;* ⓞ orcid.org/0000-0002-1900-0030

XiangHua Zhang − *Institut des Sciences Chimiques de Rennes UMR 6226, Université de Rennes 1, Rennes 35042, France*

Complete contact information is available at:

https://pubs.acs.org/10.1021/acsaem.9b02192

REFERENCES

(1) Chu, S.; Majumdar, A. Opportunities and Challenges for a Sustainable Energy Future. *Nature* **2012**, *488* (7411), 294−303.

(2) Burst, J. M.; Duenow, J. N.; Albin, D. S.; Colegrove, E.; Reese, M. O.; Aguiar, J. A.; Jiang, C.-S.; Patel, M. K.; Al-Jassim, M. M.; Kuciauskas, D.; Swain, S.; Ablekim, T.; Lynn, K. G.; Metzger, W. K. CdTe Solar Cells with Open-Circuit Voltage Breaking the 1 V Barrier. *Nat. Energy* **2016**, *1* (3), 16015.

(3) Zhao, Y.; Boccard, M.; Liu, S.; Becker, J.; Zhao, X.-H.; Campbell, C. M.; Suarez, E.; Lassise, M. B.; Holman, Z.; Zhang, Y.-H. Monocrystalline CdTe Solar Cells with Open-Circuit Voltage over 1 V and Efficiency of 17%. *Nat. Energy* **2016**, *1* (6), 16067.

(4) Zhou, Y.; Leng, M.; Xia, Z.; Zhong, J.; Song, H.; Liu, X.; Yang, B.; Zhang, J.; Chen, J.; Zhou, K.; Han, J.; Cheng, Y.; Tang, J. Solution-Processed Antimony Selenide Heterojunction Solar Cells. *Adv. Energy Mater.* **2014**, *4* (8), 1301846.

(5) Leng, M.; Luo, M.; Chen, C.; Qin, S.; Chen, J.; Zhong, J.; Tang, J. Selenization of Sb_2Se_3 Absorber Layer: An Efficient Step to Improve Device Performance of CdS/Sb_2Se_3 Solar Cells. *Appl. Phys. Lett.* **2014**, *105* (8), 083905.

(6) Liu, X.; Chen, C.; Wang, L.; Zhong, J.; Luo, M.; Chen, J.; Xue, D.-J.; Li, D.; Zhou, Y.; Tang, J. Improving the Performance of Sb_2Se_3 Thin Film Solar Cells over 4% by Controlled Addition of Oxygen during Film Deposition. *Prog. Photovoltaics* **2015**, *23* (12), 1828−1836.

(7) Chen, C.; Zhao, Y.; Lu, S.; Li, K.; Li, Y.; Yang, B.; Chen, W.; Wang, L.; Li, D.; Deng, H.; Yi, F.; Tang, J. Accelerated Optimization of TiO_2/Sb_2Se_3 Thin Film Solar Cells by High-Throughput Combinatorial Approach. *Adv. Energy Mater.* **2017**, *7* (20), 1700866.

(8) Liu, X.; Xiao, X.; Yang, Y.; Xue, D.-J.; Li, D.-B.; Chen, C.; Lu, S.; Gao, L.; He, Y.; Beard, M. C.; Wang, G.; Chen, S.; Tang, J. Enhanced Sb_2Se_3 Solar Cell Performance through Theory-Guided Defect Control. *Prog. Photovoltaics* **2017**, *25* (10), 861−870.

(9) Chen, C.; Wang, L.; Gao, L.; Nam, D.; Li, D.; Li, K.; Zhao, Y.; Ge, C.; Cheong, H.; Liu, H.; Song, H.; Tang, J. 6.5% Certified Efficiency Sb_2Se_3 Solar Cells Using PbS Colloidal Quantum Dot Film as Hole-Transporting Layer. *ACS Energy Lett.* **2017**, *2* (9), 2125−2132.

(10) Chen, C.; Li, K.; Chen, S.; Wang, L.; Lu, S.; Liu, Y.; Li, D.; Song, H.; Tang, J. Efficiency Improvement of Sb 2 Se 3 Solar Cells via Grain Boundary Inversion. *ACS Energy Lett.* **2018**, *3* (10), 2335−2341.

(11) Li, Z.; Liang, X.; Li, G.; Liu, H.; Zhang, H.; Guo, J.; Chen, J.; Shen, K.; San, X.; Yu, W.; Schropp, R. E. I.; Mai, Y. 9.2%-Efficient Core-Shell Structured Antimony Selenide Nanorod Array Solar Cells. *Nat. Commun.* **2019**, *10* (1), 125.

(12) Petzelt, J.; Grigas, J. Far Infrared Dielectric Dispersion in Sb_2S_3, Bi_2S_3 and Sb_2Se_3 Single Crystals. *Ferroelectrics* **1973**, *5* (1), 59−68.

(13) Chen, C.; Bobela, D. C.; Yang, Y.; Lu, S.; Zeng, K.; Ge, C.; Yang, B.; Gao, L.; Zhao, Y.; Beard, M. C.; Tang, J. Characterization of Basic Physical Properties of Sb_2Se_3 and Its Relevance for Photovoltaics. *Front. Optoelectron.* **2017**, *10* (1), 18−30.

(14) Chen, C.; Li, W.; Zhou, Y.; Chen, C.; Luo, M.; Liu, X.; Zeng, K.; Yang, B.; Zhang, C.; Han, J.; Tang, J. Optical Properties of Amorphous and Polycrystalline Sb_2Se_3 Thin Films Prepared by Thermal Evaporation. *Appl. Phys. Lett.* **2015**, *107* (4), 043905.

(15) Filip, M. R.; Patrick, C. E.; Giustino, F. GW Quasiparticle Band Structures of Stibnite, Antimonselite, Bismuthinite, and Guanajuatite. *Phys. Rev. B: Condens. Matter Mater. Phys.* **2013**, *87* (20), 205125.

(16) Patrick, C. E.; Giustino, F. Structural and Electronic Properties of Semiconductor-Sensitized Solar-Cell Interfaces. *Adv. Funct. Mater.* **2011**, *21* (24), 4663−4667.

(17) Huang, M.; Xu, P.; Han, D.; Tang, J.; Chen, S. Complicated and Unconventional Defect Properties of the Quasi-One-Dimensional Photovoltaic Semiconductor Sb_2Se_3. *ACS Appl. Mater. Interfaces* **2019**, *11* (17), 15564−15572.

(18) Perdew, J. P.; Burke, K.; Ernzerhof, M. Generalized Gradient Approximation Made Simple. *Phys. Rev. Lett.* **1996**, *77* (18), 3865−3868.

(19) Kresse, G.; Furthmüller, J. Efficient Iterative Schemes for Ab Initio Total-Energy Calculations Using a Plane-Wave Basis Set. *Phys. Rev. B: Condens. Matter Mater. Phys.* **1996**, *54* (16), 11169−11186.

(20) Kresse, G.; Furthmüller, J. Efficiency of Ab-Initio Total Energy Calculations for Metals and Semiconductors Using a Plane-Wave Basis Set. *Comput. Mater. Sci.* **1996**, *6* (1), 15−50.

(21) Kresse, G.; Joubert, D. From Ultrasoft Pseudopotentials to the Projector Augmented-Wave Method. *Phys. Rev. B: Condens. Matter Mater. Phys.* **1999**, *59* (3), 1758−1775.

(22) Savory, C. N.; Scanlon, D. O. The Complex Defect Chemistry of Antimony Selenide. *J. Mater. Chem. A* **2019**, *7* (17), 10739−10744.

(23) Grimme, S.; Ehrlich, S.; Goerigk, L. Effect of the Damping Function in Dispersion Corrected Density Functional Theory. *J. Comput. Chem.* **2011**, *32* (7), 1456−1465.

(24) Grimme, S.; Antony, J.; Ehrlich, S.; Krieg, H. A Consistent and Accurate Ab Initio Parametrization of Density Functional Dispersion Correction (DFT-D) for the 94 Elements H-Pu. *J. Chem. Phys.* **2010**, *132* (15), 154104.

(25) Monkhorst, H. J.; Pack, J. D. Special Points for Brillouin-Zone Integrations. *Phys. Rev. B* **1976**, *13* (12), 5188−5192.

(26) Kyono, A.; Hayakawa, A.; Horiki, M. Selenium Substitution Effect on Crystal Structure of Stibnite (Sb_2S_3). *Phys. Chem. Miner.* **2015**, *42* (6), 475−490.

(27) Stoliaroff, A.; Jobic, S.; Latouche, C. PyDEF 2.0: An Easy to Use Post-Treatment Software for Publishable Charts Featuring a Graphical User Interface. *J. Comput. Chem.* **2018**, *39* (26), 2251−2261.

(28) Péan, E.; Vidal, J.; Jobic, S.; Latouche, C. Presentation of the PyDEF Post-Treatment Python Software to Compute Publishable Charts for Defect Energy Formation. *Chem. Phys. Lett.* **2017**, *671*, 124−130.

(29) Brese, N. E.; O'Keeffe, M. Bond-Valence Parameters for Solids. *Acta Crystallogr., Sect. B: Struct. Sci.* **1991**, *47* (2), 192−197.

(30) Zhang, L.; Li, Y.; Li, C.; Chen, Q.; Zhen, Z.; Jiang, X.; Zhong, M.; Zhang, F.; Zhu, H. Scalable Low-Band-Gap Sb_2Se_3 Thin-Film Photocathodes for Efficient Visible-Near-Infrared Solar Hydrogen Evolution. *ACS Nano* **2017**, *11* (12), 12753−12763.

(31) Vadapoo, R.; Krishnan, S.; Yilmaz, H.; Marin, C. Electronic Structure of Antimony Selenide (Sb_2Se_3) from GW Calculations. *Phys. Status Solidi B* **2011**, *248* (3), 700−705.

(32) Li, G.; Li, Z.; Liang, X.; Guo, C.; Shen, K.; Mai, Y. Improvement in Sb 2 Se 3 Solar Cell Efficiency through Band Alignment Engineering at the Buffer/Absorber Interface. *ACS Appl. Mater. Interfaces* **2019**, *11* (1), 828−834.

(33) Tao, J.; Hu, X.; Xue, J.; Wang, Y.; Weng, G.; Chen, S.; Zhu, Z.; Chu, J. Investigation of Electronic Transport Mechanisms in Sb_2Se_3 Thin-Film Solar Cells. *Sol. Energy Mater. Sol. Cells* **2019**, *197*, 1−6.

(34) Fahey, P. M.; Griffin, P. B.; Plummer, J. D. Point Defects and Dopant Diffusion in Silicon. *Rev. Mod. Phys.* **1989**, *61* (2), 289−384.

(35) Chen, S.; Qiao, X.; Zheng, Z.; Cathelinaud, M.; Ma, H.; Fan, X.; Zhang, X. Enhanced Electrical Conductivity and Photoconductive Properties of Sn-Doped Sb_2Se_3 Crystals. *J. Mater. Chem. C* **2018**, *6* (24), 6465−6470.

(36) Stoliaroff, A.; Jobic, S.; Latouche, C. New Insights into the Determination of Maximum Chemical Potentials to Account for Alkali Doping in β-In_2S_3 by Ab Initio Calculations. *Comput. Mater. Sci.* **2019**, *168*, 221−228.

(37) Zhou, Y.; Wang, L.; Chen, S.; Qin, S.; Liu, X.; Chen, J.; Xue, D.-J.; Luo, M.; Cao, Y.; Cheng, Y.; Sargent, E. H.; Tang, J. Thin-Film Sb_2Se_3 Photovoltaics with Oriented One-Dimensional Ribbons and Benign Grain Boundaries. *Nat. Photonics* **2015**, *9* (6), 409−415.

(38) Zhang, X.; Xu, Y.; Shen, Q.; Fan, B.; Qiao, X.; Fan, X.; Yang, H.; Luo, Q.; Calvez, L.; Ma, H.; Cathelinaud, M.; Simon, J.-J. Enhancement of Charge Photo-Generation and Transport via an Internal Network of Sb_2Se_3/Cu_2GeSe_3 Heterojunctions. *J. Mater. Chem. A* **2014**, *2* (40), 17099−17106.

Supplementary information

Deciphering the role of key defects in Sb$_2$Se$_3$, a promising candidate for chalcogenide based solar cells

Adrien Stoliaroff,[a] Alicia Lecomte,[b] Oleg Rubel,[c] Stéphane Jobic,[a] XiangHua Zhang[b], Camille Latouche[a*] and Xavier Rocquefelte [b*]

[a] Institut des Matériaux Jean Rouxel (IMN), Université de Nantes, CNRS, 2 rue de la Houssinière, BP 32229, 44322 Nantes cedex 3, France
[b] Institut des Sciences Chimiques de Rennes UMR 6226, Université de Rennes 1, Campus de Beaulieu, 35042 Rennes, France
[c] Department of Materials Science and Engineering, McMaster University, 1280 Main Street West, Hamilton, Ontario L8S 4L8, Canada
camille.latouche@univ-nantes.fr ; xavier.rocquefelte@univ-rennes1.fr

Simulating dispersion forces

We compare different methodologies to account for the dispersion forces, including or not Becke-Johnson damping factor. **10.1002/jcc.21759** Without any dispersion, PBE significantly (+8.0%) overestimates the *a* parameter, highlighting the need for dispersion corrections. GD3 scheme performs much better with a deviation on cell parameters with respect to experiment inferior to 2%. GD3-BJ overcorrects dispersion effects and lead to a systematic underestimation of cell parameters. This is particularly visible on the volume of the cell. These figures convince us to use PBE + GD3 for the study of defects.

Table S1. Comparison of cell parameters computed with different dispersion corrections with respect to experimental structure, relative deviation in brackets. 10.1007/s00269-015-0737-x.

	a (Å)	b (Å)	c (Å)	V (Å^3)
Exp.	11.805	3.988	11.662	549
PBE	12.753	4.028	11.539	592.75
	(8.0%)	(1.0%)	(-1.1%)	(8.0%)
PBE + GD3	12.015	4.019	11.465	553.7
	(1.8%)	(0.8%)	(-1.7%)	(0.9%)

PBE + GD3-BJ	11.682 (-1.0%)	3.986 (0.0%)	11.329 (-2.9%)	527.49 (-3.9%)

Table S2 VSe_1 defect formation enthalpy with respect to supercell size. The difference is negligible, proving that a 1x3x1 supercell is suitable for the defect study.

Supercell size	Charge	$\Delta H_f(\mu_{E_F}=0)(eV)$ Se-rich/Sb-poor	Se-poor/Sb-rich	$\varepsilon_{+2/0}$ (eV)
1x3x1	q=0	1.584	1.137	0.55
	q=+2	0.489	0.042	
2x3x2	q=0	1.502	1.055	0.59
	q=+2	0.331	-0.116	

Table S3 Calculated Fermi levels and free carrier concentrations at T_{growth}= 800K and T_{room}= 300K. For each dopant, all defects related to this dopant along with all intrinsic defects were taken into account for the calculation.

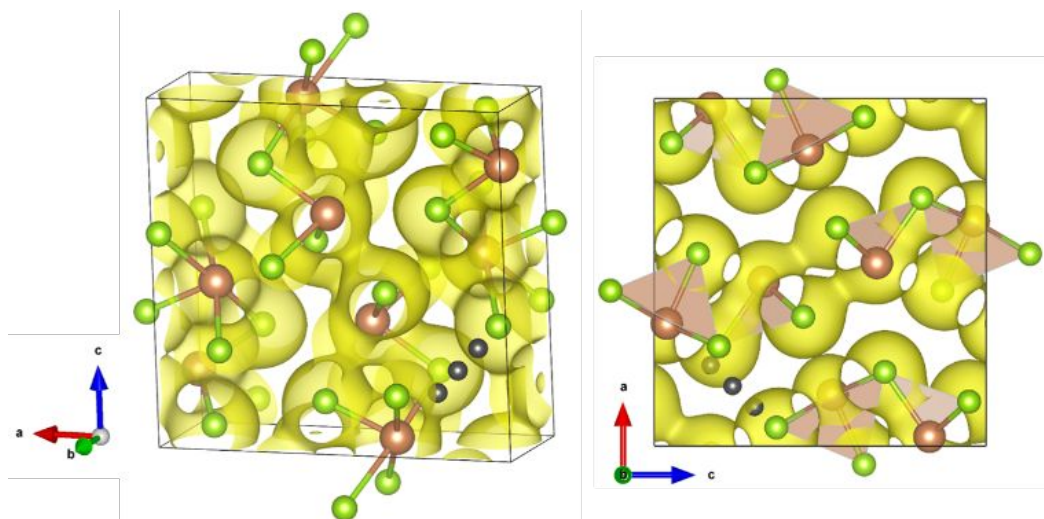|	E_F^{growth} (eV)	E_F^{room} (eV)	n_h (cm-3)	n_e (cm-3)
	Se-poor/Sb-rich			
Intrinsics	0.43	0.12	3.8E+16	1.2E+00
Tin	0.29	0.07	2.9E+17	1.6E-01
Copper	0.60	0.22	1.0E+15	4.6E+01
Chlorine	0.78	1.10	1.4E+00	3.4E+16
Bromide	0.75	1.09	2.2E+00	2.1E+16
Iodine	0.67	1.06	7.9E+00	5.9E+15
	Se-rich/Sb-poor			
Intrinsics	0.55	0.17	5.4E+15	8.6E+00
Tin	0.22	0.04	7.6E+17	5.8E-02
Copper	0.44	0.13	3.4E+16	1.4E+00
Chlorine	0.68	1.06	6.8E+00	6.9E+15
Bromide	0.67	1.05	8.8E+00	5.3E+15
Iodine	0.63	1.02	3.0E+01	1.6E+15

Figure S1. Charge density isosurfaces (yellow) in ideal Sb_2Se_3 conventional cell. Black dots highlight a low density region along a (0.30, 0, -0.33) vector.
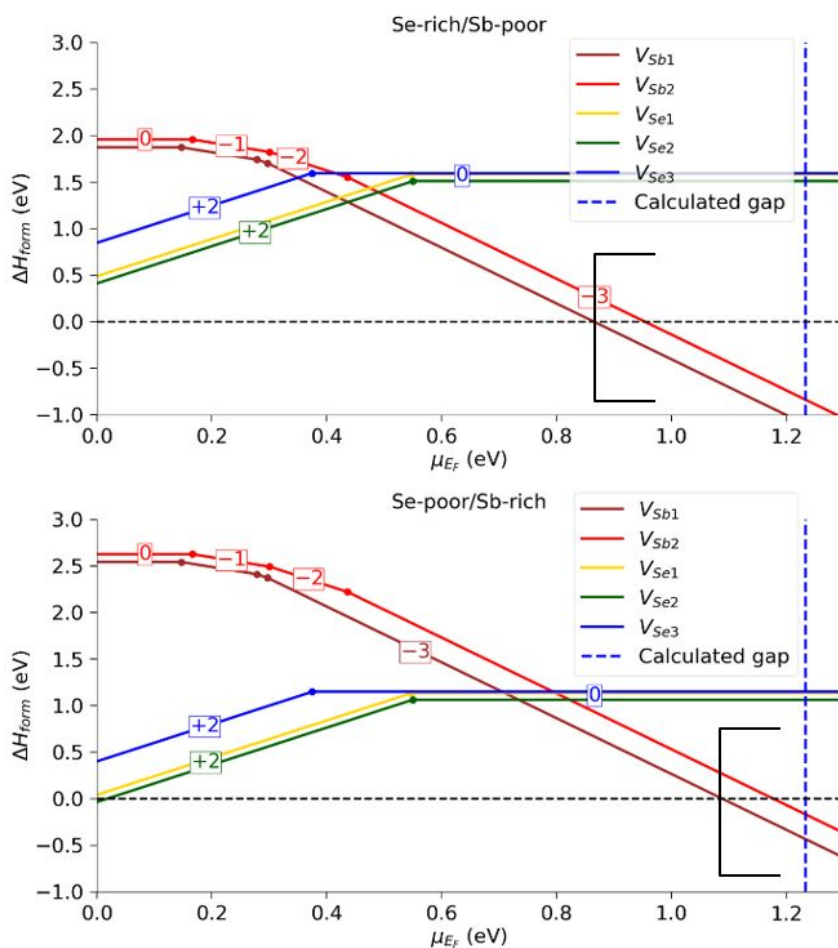

Figure S2. Formation enthalpies of the vacancies *vs.* Fermi level. Each line corresponds to the charge (encapsulated) exhibiting the lowest formation enthalpy. Points mark transition levels. Brackets highlight the dopability limit.
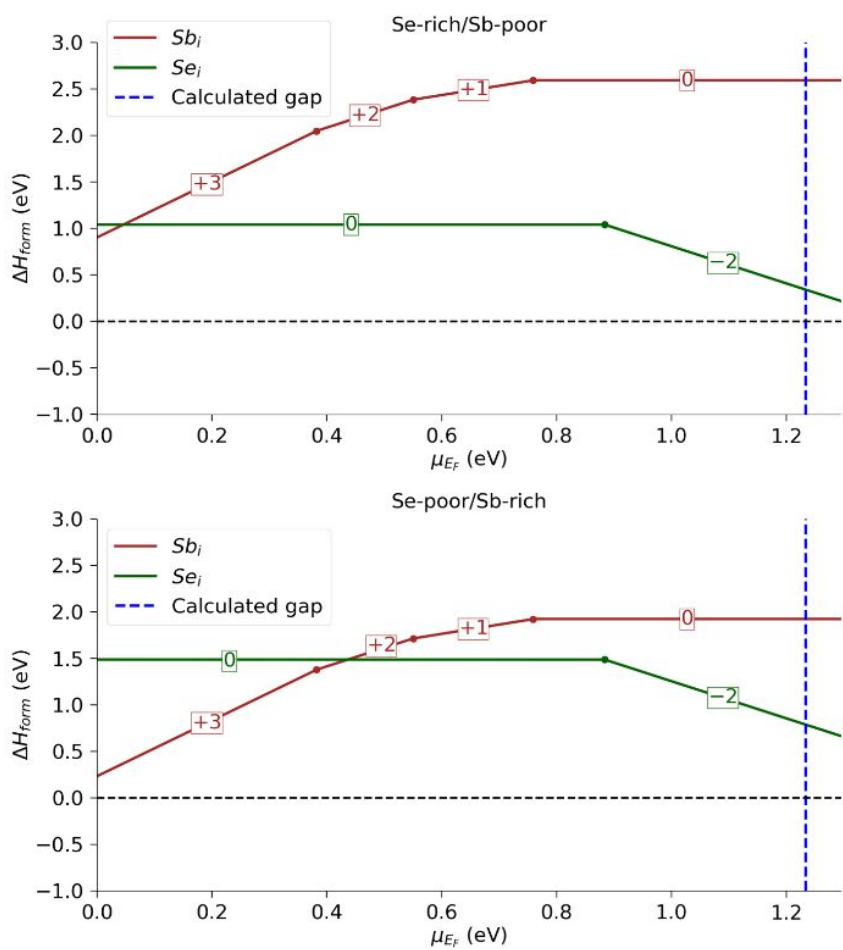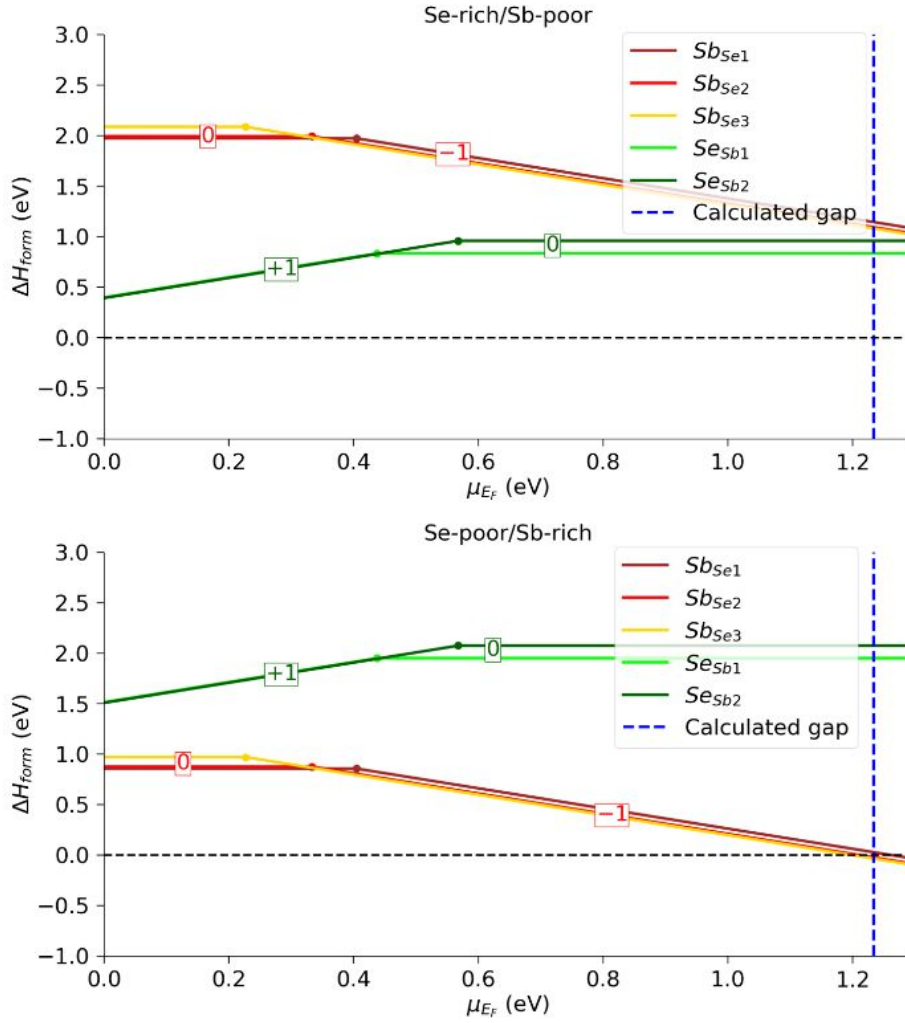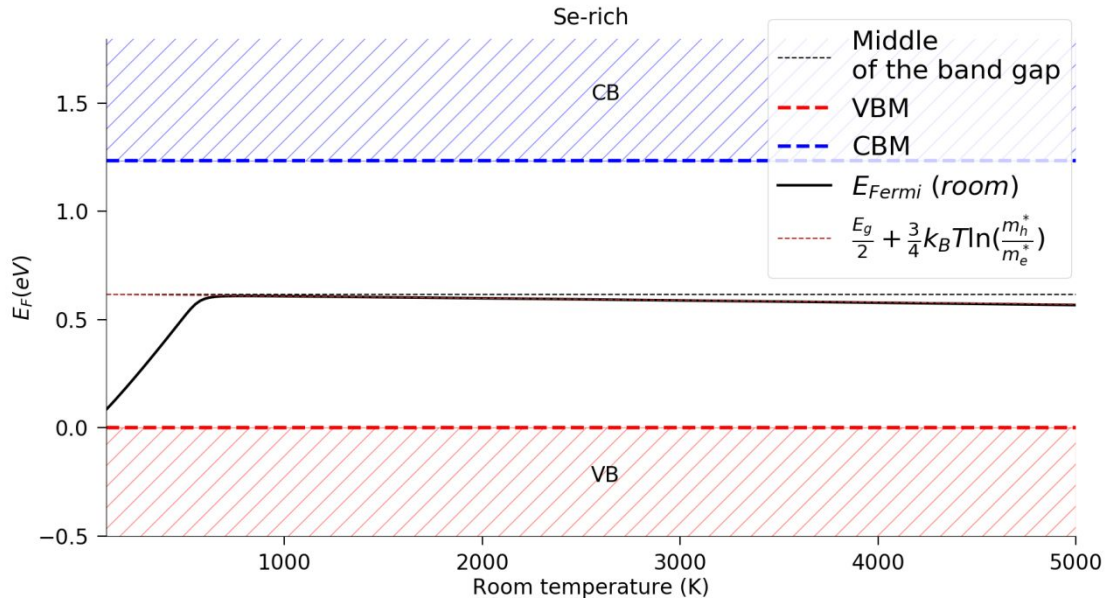
Figure S3. Formation enthalpies of Sb and Se interstitials *vs.* Fermi level. Each line corresponds to the charge (encapsulated) exhibiting the lowest formation enthalpy. Points mark transition levels.

Figure S4. Formation enthalpies of antisites in Sb_2Se_3 *vs.* Fermi level. Each line corresponds to the charge (encapsulated) exhibiting the lowest formation enthalpy. Points mark transition levels.

Figure S5 Simulated Fermi level as a function of operating temperature for a model synthesis temperature of 550 K in Se-rich/Sb-poor synthesis conditions. (E_F increases with T shifting from a freeze out regime to an intrinsic one). Theoretical trend in brown.
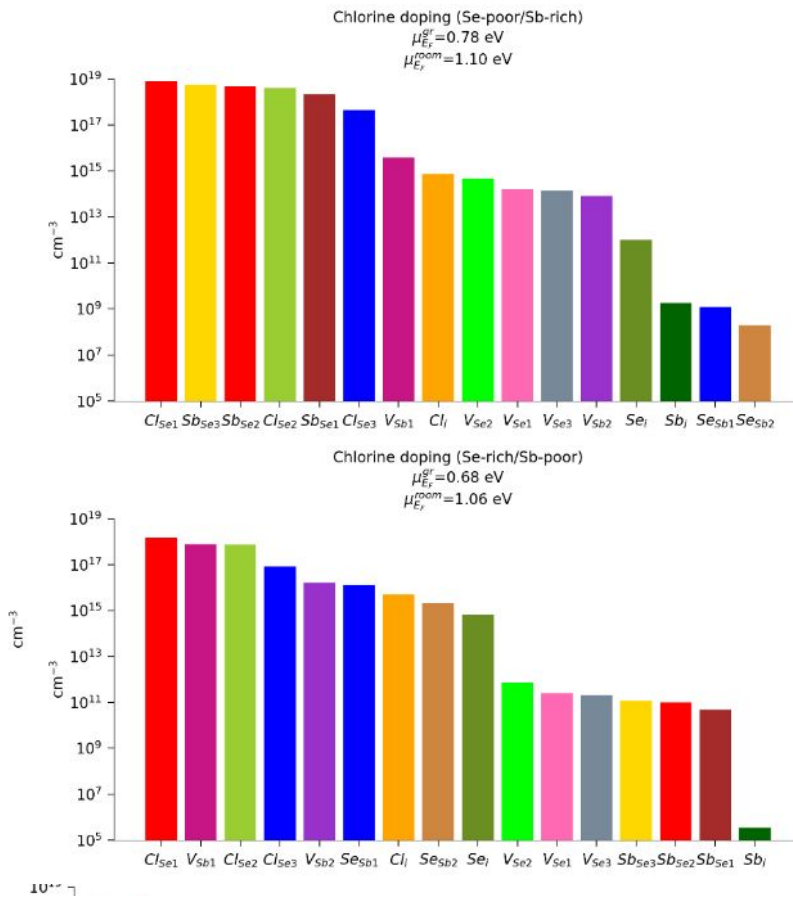

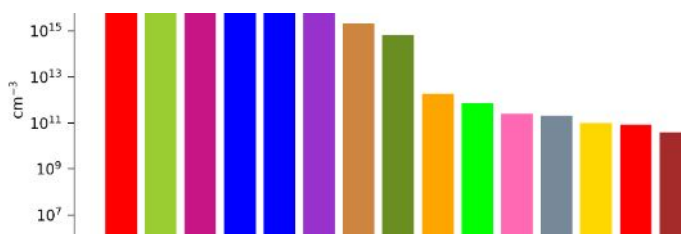**Figure S6** Estimated defect concentrations for chlorine doping at T_{growth}= 800K.

Figure S7 Estimated defect concentrations for bromine doping at T_{growth}= 800K.